

A thermodynamic framework for unified continuum models for the healing of damaged soft biological tissue

Di Zuo^a, Yiqian He^{a,*}, Stéphane Avril^c, Haitian Yang^a, Klaus Hackl^b

^a*State Key Lab of Structural Analysis for Industrial equipment, Department of Engineering Mechanics, Dalian University of Technology, Dalian 116024, P.R. China*

^b*Mechanik-Materialtheorie, Ruhr-Universität Bochum, Bochum, Germany*

^c*Mines Saint-Etienne, University of Lyon, University Jean Monnet, Inserm, Sainbiose U1059, F-42023 Saint-Etienne, France*

Abstract

When they are damaged or injured, soft biological tissues are able to self-repair and heal. Mechanics is critical during the healing process, as the damaged extracellular matrix (ECM) tends to be replaced with a new undamaged ECM supporting homeostatic stresses. Computational modeling has been commonly used to simulate the healing process. However, there is a pressing need to have a unified thermodynamics theory for healing. From the viewpoint of continuum damage mechanics, some key parameters related to healing processes, for instance, the volume fraction of newly grown soft tissue and the growth deformation, can be regarded as internal variables and have related evolution equations. This paper is aiming to establish this unified framework inspired by thermodynamics for continuum damage models for the healing of soft biological tissues. The significant advantage of the proposed model is that no *ad hoc* equations are required for describing the healing process. Therefore, this new model is more concise and offers a universal approach to simulate the healing process. Three numerical examples are provided to demonstrate the effectiveness of the proposed model, which is in good agreement with the existing works, including an application for balloon angioplasty in an arteriosclerotic artery with a fiber cap.

Keywords: Healing, Soft biological tissue, Continuum damage model, Unified models, Thermodynamic framework

1. Introduction

Soft biological tissue, such as arteries, skin, ligaments, and tendons, has the ability to grow and change through the formation of new constituents and the removal of old constituents [1]. Understanding the underlying mechanisms of the healing of damaged soft tissue has important applications, for instance, the accurate prediction of the rupture risk of an aortic aneurysm is critical to improve clinical treatment planning [2], the understanding

*Corresponding author: heyiqian@dlut.edu.cn

of short-term and long-term damage evolution in the interaction with medical devices for soft tissue is essential for the optimization of these devices [2], and the modeling of wound healing in the skin can improve wound and scar treatment [3, 4].

The healing of soft biological tissue is a complex biochemical and biomechanical process of self-recovering or self-repairing the injured or damaged extracellular matrix (ECM), and is usually divided into four stages: haemostasis, inflammation, proliferation, and remodeling. These four stages were described in great detail by Comellas et al. [4] and Cumming et al. [5]. It was reported that the first three stages (from haemostasis to proliferation) may last several weeks and that the final stage of remodeling may last from weeks to years. This last stage consists of continuous turnover (synthesis and degradation) of the ECM simultaneously with the production of scar tissue. The mechanical loading is to be proved to have a significant impact on the speed and efficiency of healing, although the underlying detailed mechanobiological mechanisms involved are not fully clear [4].

Computational modeling can provide insight into the healing of soft tissues from both short-term and long-term perspectives, and has become more popular for intense research, since experimental research is very time consuming and always involves ethical issues arising from the use of living samples. Generally, there are two types of approaches [3, 6]: The first type focuses on the underlying cellular and biochemical mechanisms based on continuum or hybrid discrete/continuum approaches, including the simulation of wound contraction [6, 7] and angiogenesis [8], providing means to reveal the underlying mechanism, usually from a microscopic view. The other type, more phenomenological, focuses on the change in the material properties of tissue during the remodeling phase. For instance, Comellas et al. developed a homeostasis-driven turnover remodeling model for healing in soft tissues based on continuum damage mechanics [4]. Moreover, some studies focus on modeling the specified remodeling process, e.g., the collagen fiber reorientation [9], continuous turnover of constituents [9] and constrained mixture computational method [10, 11, 12].

Despite the existing works introduced above, the computational modeling of healing is still challenging, a main drawback of the current healing models being that some *ad hoc* equations, based on different assumptions, have to be employed to describe the change in variables, resulting in a significant increase in modeling complexity. Continuum damage mechanics (CDM), which is consistent with an open-system thermodynamics framework, provides a powerful approach to capture the continuous turnover of tissue. In our previous work [13, 14], a nonlocal continuum healing model was presented by combining a gradient-enhanced damage model and a temporally homogenized G&R model. Instead of introducing a mechanobiological model to describe the G&R process, e.g., the temporally homogenized growth and remodeling (G&R) model, a more general and unified approach is newly presented in this paper. The core idea is that, from the viewpoint of CDM, the parameters related to the healing process can be regarded as internal variables, in the same way as the damage variable. Therefore, it is possible to establish a more rigorous and concise unified model without any *ad hoc* equations, including the evolution equations for the growth and remodeling based on strict thermodynamic considerations. To the best of the authors' knowledge, there appears to be no work related to the model proposed in this paper to date.

Based on the above considerations, a new unified continuum damage model is first es-

tablished in this paper. The proposed theoretical framework provides a more convenient computational model without any *ad hoc* equations. A numerical simulation based on the newly established damage models will result in a powerful tool for predicting and understanding the mechanism of the self-healing behavior in soft biological tissues, particularly in regard to diseases or wounds such as aneurysms or skin wounds, and will help to improve related treatment methods.

The paper is organized as follows: Section 2 introduces the framework of the unified damage model for healing, including the basic kinematics in Section 2.1, thermodynamic modeling of growth in Section 2.2, coupling to remodeling in Section 2.3, coupling to damage in Section 2.4, summary of the evolution equations of healing in Section 2.5, gradient-enhanced nonlocal damage model in Section 3, total potential energy and variational form in Section 4.2, and constitutive model in Section 4.1. Section 5 provides numerical examples to demonstrate the effectiveness of the proposed model. Finally, discussions and conclusions are given in Section 6.

2. The thermodynamic framework of the unified damage model for healing

2.1. Basic kinematics

Let $\boldsymbol{x} = \boldsymbol{\varphi}(\boldsymbol{X}, t)$ describe the motion of the. This equation transforms referential placements $\boldsymbol{x} \in \kappa(0)$ into their spatial counterparts $\boldsymbol{x} \in \kappa(t)$, where $\kappa(0)$ and $\kappa(t)$ are the initial reference configuration and current configuration, respectively. The deformation gradient and the Jacobian, which maps the referential volume dV onto the current volume dv , are defined as

$$\boldsymbol{F} = \nabla_{\boldsymbol{x}} \boldsymbol{\varphi}, \quad (1)$$

$$J = \frac{dv}{dV} = \det(\boldsymbol{F}). \quad (2)$$

We introduce a variational approach for the description of inelastic processes that rests on thermodynamic extremal principles. For this purpose, let us consider a physical system described by (sets of) external, i.e., controllable, state variables, in our case given by the deformation gradient \boldsymbol{F} , and internal state variables \boldsymbol{z} .

We assume that the system behavior may be defined using only two scalar potentials: free energy $\psi(\boldsymbol{F}, \boldsymbol{z})$ and dissipation potential $\Delta(\boldsymbol{z}, \dot{\boldsymbol{z}})$. The deformation \boldsymbol{x} is given by the minimization of energy as

$$\inf_{\boldsymbol{x}} \left\{ \int_{\Omega} \psi(\boldsymbol{F}, \boldsymbol{z}) dV + f_{\text{ext}}(\boldsymbol{x}) | \boldsymbol{x} = \boldsymbol{x}_0 \text{ on } \partial\Omega \right\}, \quad (3)$$

where $f_{\text{ext}}(\boldsymbol{x})$ denotes the potential of external driving forces. The evolution of the internal variables is described by the Biot equation.

$$\frac{\partial \psi}{\partial \boldsymbol{z}} + \frac{\partial \Delta}{\partial \dot{\boldsymbol{z}}} = \mathbf{0}. \quad (4)$$

Note that Eq. (4) may be written as a stationarity condition of the minimization problem

$$\inf_{\dot{\mathbf{z}}} \left\{ \dot{\Psi} + \Delta \right\}. \quad (5)$$

2.2. Thermodynamic modeling of growth

Let us assume that the local state of tissue growth is given by an internal variable of an inelastic deformation gradient $\mathbf{z} = \mathbf{F}_g$, such that the total deformation gradient is given as

$$\mathbf{F} = \mathbf{F}_e \cdot \mathbf{F}_g, \quad (6)$$

where \mathbf{F}_e denotes the part of the deformation gradient given by elastic straining. The elastic free energy depends on \mathbf{F}_e only. Hence we have

$$\psi_{\text{el}}(\mathbf{F}_e) = \psi_{\text{el}}(\mathbf{F} \cdot \mathbf{F}_g^{-1}). \quad (7)$$

In a material that has already undergone growth, the free energy must be related to the volume of the grown tissue, i.e., premultiplied by $J_g = \det(\mathbf{F}_g)$. Moreover, we introduce a constant term $\Delta\psi_{\text{ph}}$ contained in the free energy, which we denote as the physiological potential. We assume that $\Delta\psi_{\text{ph}}$ can be influenced by physiological processes to stimulate growth where necessary. With this notion, the free energy takes the form

$$\psi(\mathbf{F}, \mathbf{F}_g) = J_g \left(\psi_{\text{el}}(\mathbf{F} \cdot \mathbf{F}_g^{-1}) + \Delta\psi_{\text{ph}} \right). \quad (8)$$

We obtain the first Piola-Kirchhoff stress tensor as

$$\mathbf{P} = \frac{\partial \psi}{\partial \mathbf{F}} = J_g \frac{\partial \psi_{\text{el}}}{\partial \mathbf{F}_e} \cdot \mathbf{F}_g^{-\text{T}}, \quad (9)$$

and the Cauchy stress tensor as

$$\boldsymbol{\sigma} = \frac{1}{J} \mathbf{P} \cdot \mathbf{F}^{\text{T}} = \frac{1}{J_e} \frac{\partial \psi_{\text{el}}}{\partial \mathbf{F}_e} \cdot \mathbf{F}_e^{\text{T}}, \quad (10)$$

where $J = \det(\mathbf{F})$ and $J_e = \det(\mathbf{F}_e)$. Material frame indifference requires that ψ_{el} factors through the right Cauchy-Green tensor $\mathbf{C}_e = \mathbf{F}_e^{\text{T}} \cdot \mathbf{F}_e$. Employing the relation

$$\frac{\partial \psi_{\text{el}}}{\partial \mathbf{F}_e} = 2 \mathbf{F}_e \cdot \frac{\partial \psi_{\text{el}}}{\partial \mathbf{C}_e}, \quad (11)$$

we obtain

$$\boldsymbol{\sigma} = \frac{1}{J_e} 2 \mathbf{F}_e \cdot \frac{\partial \psi_{\text{el}}}{\partial \mathbf{C}_e} \cdot \mathbf{F}_e^{\text{T}}, \quad (12)$$

where $\boldsymbol{\sigma}$ is indeed symmetric. Note that $\boldsymbol{\sigma}$ depends on \mathbf{F}_e only.

We introduce a thermodynamic driving force associated with growth by

$$\mathbf{q}_g = - \frac{\partial \psi}{\partial \mathbf{F}_g}. \quad (13)$$

Employing Eq. (9) and the fact, that $\frac{\partial J_g}{\partial \mathbf{F}_g} = J_g \mathbf{F}_g^{-\text{T}}$, we obtain

$$\mathbf{q}_g = -\mathbf{F}_g^{-\text{T}} \cdot (\psi \mathbf{I} - \mathbf{F}^{\text{T}} \cdot \mathbf{P}). \quad (14)$$

Note that $\mathbf{b} = \psi \mathbf{I} - \mathbf{F}^{\text{T}} \cdot \mathbf{P}$ is the Eshelby stress tensor known to be associated with the configuration change.

To close our model, we still have to introduce a dissipation potential. Because we have to respect the material frame indifference once again, we have to formulate this by employing an objective rate. A straightforward choice is the velocity gradient $\mathbf{L}_g = \dot{\mathbf{F}}_g \cdot \mathbf{F}_g^{-1}$. With this notion, we define the dissipation potential as

$$\Delta_g(\mathbf{L}_g) = J_g \left(r_g \|\mathbf{L}_g\| + \frac{1}{2M_g} \|\mathbf{L}_g\|^2 \right). \quad (15)$$

Note that, similar to the free energy, the dissipation potential has to be premultiplied by J_g . Because of the non-differentiability of Δ at $\mathbf{L}_g = \mathbf{0}$, Eq. (4) becomes a differential inclusion and takes the form

$$\mathbf{q}_g \in J_g \left(r_g \text{sign } \mathbf{L}_g + \frac{1}{M_g} \mathbf{L}_g \right) \cdot \mathbf{F}_g^{-\text{T}}, \quad (16)$$

which has the solution

$$\mathbf{L}_g = M_g \left(\frac{1}{J_g} \|\mathbf{q}_g \cdot \mathbf{F}_g^{\text{T}}\| - r_g \right)_+ \text{sign}(\mathbf{q}_g \cdot \mathbf{F}_g^{\text{T}}), \quad (17)$$

where $(\cdot)_+$ denotes the positive part of the argument. The set-valued sign function of a tensor \mathbf{T} is defined as

$$\text{sign}(\mathbf{T}) = \begin{cases} \{\mathbf{S}, \|\mathbf{S}\| \leq 1\} & \text{for } \mathbf{T} = \mathbf{0} \\ \left\{ \frac{1}{\|\mathbf{T}\|} \mathbf{T} \right\} & \text{for } \mathbf{T} \neq \mathbf{0} \end{cases}. \quad (18)$$

We see that M_g plays the role of a mobility controlling the velocity of the growth process, and r_g corresponds to a growth limit that is related to a homeostatic state.

A brief calculation gives

$$\bar{\mathbf{q}}_g := \frac{1}{J_g} \mathbf{q}_g \cdot \mathbf{F}_g^{\text{T}} = -(\psi_{\text{el}} + \Delta\psi_{\text{ph}}) \mathbf{I} + \mathbf{F}_e^{\text{T}} \cdot \frac{\partial \psi_{\text{el}}}{\partial \mathbf{F}_e}, \quad (19)$$

and Eq. (17) becomes

$$\mathbf{L}_g = M_g (\|\bar{\mathbf{q}}_g\| - r_g)_+ \text{sign}(\bar{\mathbf{q}}_g). \quad (20)$$

Note that $\bar{\mathbf{q}}_g$ depends on \mathbf{F}_e only. Using Eqs. (11) and (12), we obtain

$$\bar{\mathbf{q}}_g = -J_e \mathbf{I} + 2 \mathbf{C}_e \cdot \frac{\partial \psi_{\text{el}}}{\partial \mathbf{C}_e} = -(\psi_{\text{el}} + \Delta\psi_{\text{ph}}) \mathbf{I} + J_e \mathbf{F}_e^{\text{T}} \cdot \boldsymbol{\sigma} \cdot \mathbf{F}_e^{-\text{T}}. \quad (21)$$

For deformations large enough in order to hold $\|\bar{\mathbf{q}}_g\| > r_g$, the driving forces tend to converge to the hypersurface given by

$$\|\bar{\mathbf{q}}_g\| = r_g, \quad (22)$$

defining a yield condition for growth. Let us investigate this hypersurface closer. A straightforward calculation gives

$$\|\bar{\mathbf{q}}_g\|^2 = 3(\psi_{\text{el}} + \Delta\psi_{\text{ph}})^2 - 2J_e(\psi_{\text{el}} + \Delta\psi_{\text{ph}}) + J_e^2 \|\mathbf{F}_e^{-1} \cdot \boldsymbol{\sigma} \cdot \mathbf{F}_e\|^2. \quad (23)$$

We see that Eq. (22) involves the Cauchy stress $\boldsymbol{\sigma}$ but in general also the elastic deformation gradient \mathbf{F}_e . Note that the physiological potential $\Delta\psi_{\text{ph}}$ shifts the growth to higher volumetric stresses.

2.2.1. The isotropic case

In this paper, only the case of isotropic growth is considered. For an isotropic tissue, the growth will be volumetric only, i.e., we have

$$\mathbf{F}_g = J_g^{1/3} \mathbf{I}. \quad (24)$$

We assume a split of the free energy into a volumetric and an isochoric part as

$$\psi_{\text{el}}(\mathbf{F}_e) = U(J_e) + \psi_{\text{iso}}(\bar{\mathbf{F}}_e), \quad (25)$$

where $\bar{\mathbf{F}}_e = J_e^{-1/3} \mathbf{F}_e$. Employing Eq. (24), we obtain

$$\bar{\mathbf{F}}_e = \bar{\mathbf{F}} = J^{-1/3} \mathbf{F}. \quad (26)$$

A brief calculation using Eq. (25) gives

$$\mathbf{P} = J_g \left(J_e U'(J_e) \mathbf{I} + J^{-1/3} \text{dev} \left(\frac{\partial \psi_{\text{iso}}}{\partial \bar{\mathbf{F}}} \cdot \bar{\mathbf{F}}^{\text{T}} \right) \right) \cdot \mathbf{F}^{-\text{T}}, \quad (27)$$

$$\boldsymbol{\sigma} = U'(J_e) \mathbf{I} + J_g J^{-4/3} \text{dev} \left(\frac{\partial \psi_{\text{iso}}}{\partial \bar{\mathbf{F}}} \cdot \bar{\mathbf{F}}^{\text{T}} \right), \quad (28)$$

$$\bar{\mathbf{q}}_g = -(\psi_{\text{el}} + \Delta\psi_{\text{ph}} + J_e U'(J_e)) \mathbf{I} = -\left(\psi_{\text{el}} + \Delta\psi_{\text{ph}} + \frac{J_e}{3} \text{tr} \boldsymbol{\sigma} \right) \mathbf{I}, \quad (29)$$

with $\text{dev}(\mathbf{T}) = \mathbf{T} - \frac{1}{3} \text{tr}(\mathbf{T}) \mathbf{I}$. For an isotropic material, ψ_{el} can be expressed as a function of the principal invariants of $\boldsymbol{\sigma}$. Hence, the yield condition given by Eq. (22) can now be formally formulated in $\boldsymbol{\sigma}$ only.

2.3. Coupling to remodeling

By remodeling, we understand the physiological replacement of one tissue by a different one. This effect can be described via our thermodynamic concept as well. For this purpose, two materials are labeled by the index $i \in 1, 2$ are considered, which having total deformation gradients \mathbf{F}_i , inelastic deformation gradients \mathbf{F}_{gi} , elastic energies ψ_{eli} , physiological potentials $\Delta\psi_{phi}$ and dissipation potentials Δ_{gi} , as defined in the previous section. The formulation can be extended to an arbitrary number of tissues in a straightforward manner.

Assume, that the first tissue exists with the volume ratio $(1 - \lambda)$ and the second one with the volume ratio λ . Moreover, suppose that both tissues have the same deformation gradient, i.e., $\mathbf{F}_1 = \mathbf{F}_2 =: \mathbf{F}$. This Taylor assumption is justified for tissues that are woven into each other and thus kinematically constrained - a situation typical for biological tissues. We obtain the total free energy

$$\begin{aligned} \psi(\mathbf{F}, \mathbf{F}_{g1}, \mathbf{F}_{g2}, \lambda) = & (1 - \lambda) J_{g1} (\psi_{el1}(\mathbf{F} \cdot \mathbf{F}_{g1}^{-1}) + \Delta\psi_{ph1}) \\ & + \lambda J_{g2} (\psi_{el2}(\mathbf{F} \cdot \mathbf{F}_{g2}^{-1}) + \Delta\psi_{ph2}). \end{aligned} \quad (30)$$

This allows us to define a thermodynamic driving force associated with remodeling as

$$q_{rm} = -\frac{\partial\psi}{\partial\lambda} = J_{g1} (\psi_{el1}(\mathbf{F} \cdot \mathbf{F}_{g1}^{-1}) + \Delta\psi_{ph1}) - J_{g2} (\psi_{el2}(\mathbf{F} \cdot \mathbf{F}_{g2}^{-1}) + \Delta\psi_{ph2}). \quad (31)$$

We see that without the presence of the physiological potentials stronger tissue with higher free energy would always be replaced by weaker tissue with lower free energy. Specifically, undamaged tissue would be replaced by damaged tissue. This would be contra-intuitive and contradict experimental observation in many cases.

To describe the evolution of the volume ration λ , we once again introduce a dissipation potential

$$\Delta_{rm}(\dot{\lambda}) = r_{rm} |\dot{\lambda}| + \frac{1}{2M_{rm}^0} \dot{\lambda}^2, \quad (32)$$

allowing us to define a total dissipation potential of the tissue as

$$\Delta(\mathbf{L}_{g1}, \mathbf{L}_{g2}, \dot{\lambda}) = (1 - \lambda) \Delta_{g1}(\mathbf{L}_{g1}) + \lambda \Delta_{g2}(\mathbf{L}_{g2}) + \Delta_{rm}(\dot{\lambda}). \quad (33)$$

Application of the thermodynamic extremal principle given in Eq. (4) will return the evolution equation Eq. (20) unchanged for \mathbf{L}_{g1} and \mathbf{L}_{g2} , respectively. For the evolution of λ , we obtain

$$\dot{\lambda} = M_{rm}^0 (|q_{rm}| - r_{rm})_+ \text{sign}(q_{rm}). \quad (34)$$

In most cases, we assume no threshold for the initiation of remodeling by setting $r_{rm} = 0$. Then Eq. (34) takes the simple form

$$\dot{\lambda} = M_{rm}^0 q_{rm}. \quad (35)$$

In addition, in many cases, the mechanical properties of the completely healed tissue remain inferior to those of uninjured tissue [15, 16]. Based on this experimental evidence, an

irreversible stiffness loss parameter η is introduced, and the remodeling mobility is redefined as

$$M_{\text{rm}}^0 = M_{\text{rm}} (\eta - \lambda)_+, \quad (36)$$

yielding the evolution equation

$$\dot{\lambda} = M_{\text{rm}} q_{\text{rm}} (\eta - \lambda)_+. \quad (37)$$

Here, $\eta = 0$ means that no damaged part can be healed and $\eta = 1.0$ means that the material can be totally healed.

2.4. Coupling to damage

The inclusion of material damage can now be easily accomplished. Let us assume material 1 to be the original tissue undergoing damage. Subsequently, it will be replaced by material 2 via remodeling during the healing process. Hence, material 2 represents “scar tissue” and is supposed to experience no further damage.

We introduce a constitutive function $f(d)$ describing the reduction in material stiffness, where d is a damage parameter and f is at least twice differentiable, monotonically decreasing and satisfies the following conditions

$$f(0) = 1, \quad \lim_{d \rightarrow \infty} f(d) = 0. \quad (38)$$

The elastic energy of material 1 is then premultiplied by $f(d)$, giving the new total energy

$$\begin{aligned} \psi(\mathbf{F}, \mathbf{F}_{\text{g1}}, \mathbf{F}_{\text{g2}}, \lambda, d) = & (1 - \lambda) J_{\text{g1}} (f(d) \psi_{\text{el1}}(\mathbf{F} \cdot \mathbf{F}_{\text{g1}}^{-1}) + \Delta\psi_{\text{ph1}}) \\ & + \lambda J_{\text{g2}} (\psi_{\text{el2}}(\mathbf{F} \cdot \mathbf{F}_{\text{g2}}^{-1}) + \Delta\psi_{\text{ph2}}). \end{aligned} \quad (39)$$

Let us study the energy in Eq. (39) for a moment. With no physiological potentials present, the damaged material is the weaker one. Hence, thermodynamics would require undamaged material to be replaced with damaged material. To prevent this, we have to set $\Delta\psi_{\text{ph1}} > 0$. Since only the difference in the physiological potentials is relevant, we set $\Delta\psi_{\text{ph2}} = 0$. However, with this setting, material 1 is replaced with material 2 even when no damage has occurred. For this reason, the physiological potential has to become a time-dependent variable $\Delta\psi_{\text{ph1}} := \Delta\psi_{\text{ph}}(t)$ and be connected to the evolution of d . This is possible only in a consistent way with respect to thermodynamics by declaring this variable to be an external one that can be influenced directly by the living body, for example, by sending messenger chemicals to the damaged tissue. We mimic this by introducing a dependence

$$\Delta\psi_{\text{ph}} = g(d), \quad (40)$$

where $g(d)$ is a positive, monotonically increasing function with $g(0) = 0$.

We obtain the thermodynamic driving force associated with damage as

$$q_{\text{d}} = -\frac{\partial\psi}{\partial d} = -(1 - \lambda) J_{\text{g1}} f'(d) \psi_{\text{el1}}(\mathbf{F} \cdot \mathbf{F}_{\text{g1}}^{-1}). \quad (41)$$

The dissipation potential associated with damage is introduced as

$$\Delta_d(\dot{d}) = r_d \dot{d} + \frac{1}{2M_d} \dot{d}^2, \quad \dot{d} \geq 0. \quad (42)$$

Note the constraint $\dot{d} \geq 0$ in Eq. (42) prohibiting any reversal of damage. We obtain a new total dissipation potential of the form

$$\Delta(\mathbf{L}_{g1}, \mathbf{L}_{g2}, \dot{\lambda}, \dot{d}) = (1 - \lambda) \left(\Delta_{g1}(\mathbf{L}_{g1}) + J_{g1} \Delta_d(\dot{d}) \right) + \lambda \Delta_{g2}(\mathbf{L}_{g2}) + \Delta_{rm}(\dot{\lambda}). \quad (43)$$

We obtain the evolution equation of damage as

$$\dot{d} = M_d \left(-f'(d) \psi_{el1}(\mathbf{F} \cdot \mathbf{F}_{g1}^{-1}) - r_d \right)_+. \quad (44)$$

Note that $-f'(d) \psi_{el1}(\mathbf{F} \cdot \mathbf{F}_{g1}^{-1}) \geq 0$.

2.5. Summary of evolution equations in healing

We summarize the obtained model in the following. Given $\mathbf{F}(t)$ we have evolution equations for the variables $\mathbf{F}_{g1}(t)$, $\mathbf{F}_{g2}(t)$, $\lambda(t)$ and $d(t)$ in the fully explicit form

$$\dot{\mathbf{F}}_{g1} \cdot \mathbf{F}_{g1}^{-1} = M_{g1} (\|\tilde{\mathbf{q}}_{g1}\| - r_{g1})_+ \text{sign}(\tilde{\mathbf{q}}_{g1}), \quad (45)$$

$$\dot{\mathbf{F}}_{g2} \cdot \mathbf{F}_{g2}^{-1} = M_{g2} (\|\tilde{\mathbf{q}}_{g2}\| - r_{g2})_+ \text{sign}(\tilde{\mathbf{q}}_{g2}), \quad (46)$$

$$\dot{\lambda} = M_{rm} (|\tilde{q}_{rm}| - r_{rm})_+ \text{sign}(\tilde{q}_{rm}), \quad (47)$$

$$\dot{d} = M_d (\tilde{q}_d - r_d)_+. \quad (48)$$

To account for the influence of damage, we introduce modified driving forces as follows:

$$\tilde{\mathbf{q}}_{g1} = - (f(d) \psi_{el1} + g(d)) \mathbf{I} + f(d) \mathbf{F}_{e1}^T \cdot \frac{\partial \psi_{el1}}{\partial \mathbf{F}_{e1}}, \quad (49)$$

$$\tilde{\mathbf{q}}_{g2} = -\psi_{el2} \mathbf{I} + \mathbf{F}_{e2}^T \cdot \frac{\partial \psi_{el2}}{\partial \mathbf{F}_{e2}}, \quad (50)$$

$$\tilde{q}_{rm} = J_{g1} (f(d) \psi_{el1}(\mathbf{F} \cdot \mathbf{F}_{g1}^{-1}) + g(d)) - J_{g2} \psi_{el2}(\mathbf{F} \cdot \mathbf{F}_{g2}^{-1}), \quad (51)$$

$$\tilde{q}_d = -f'(d) \psi_{el1}(\mathbf{F} \cdot \mathbf{F}_{g1}^{-1}). \quad (52)$$

3. Nonlocal enhancement by gradient terms

A nonlocal damage model is usually required because of the need to remove the pathological mesh dependence. Therefore, following the work of Dimitrijevic and Hackl [12, 17], a gradient-enhanced nonlocal free energy term is added to the strain energy given in Eq. (39):

$$\begin{aligned} \psi(\mathbf{F}, \mathbf{F}_{g1}, \mathbf{F}_{g2}, \lambda, d) = & (1 - \lambda) J_{g1} (f(d) \psi_{el1}(\mathbf{F} \cdot \mathbf{F}_{g1}^{-1}) + \frac{c_d}{2} \|\nabla_{\mathbf{X}} \phi\|^2 + \frac{\beta_d}{2} [\phi - \gamma_d d]^2 + \\ & \Delta \psi_{ph1}) + \lambda J_{g2} (\psi_{el2}(\mathbf{F} \cdot \mathbf{F}_{g2}^{-1}) + \Delta \psi_{ph2}). \end{aligned} \quad (53)$$

In Eq. (53), c_d represents the gradient parameter that defines the degree of gradient regularization and the internal length scale. Three other variables are introduced as well:

- the field variable ϕ , which introduces an internal length scale via its gradient occurring in the expression for the energy,

- the energy-related penalty parameter β_d , which approximately enforces the local damage field and the nonlocal field to coincide,

- parameter γ_d , which is used as a switch between the local and enhanced models.

In order to better monitor the damage and G&R process, we introduce a healing parameter $H(d, t)$ as

$$H(d, t) = (1 - \lambda)f(d) + \lambda. \quad (54)$$

The healing parameter $H(d, t)$ takes values between 0 and 1. When $H(d, t) = 0$, the tissue is completely damaged and its local stiffness is null, whereas when $H(d, t) = 1$, the tissue is completely healed with newly produced tissue replacing the previously damaged one.

4. Numerical implementation

4.1. Constitutive model

For the undamaged part ψ_0 , a neo-Hookean hyperelastic constitutive model [18] is used. It is written as

$$\psi_0 = \frac{1}{2}\mu_0 J_e^{-2/3}(I_{1e} - 3) + \frac{1}{2}\kappa_0(J_e - 1)^2, \quad (55)$$

where μ_0 and κ_0 are the shear and bulk moduli of the soft isotropic matrix, respectively. $I_{1e} = \text{tr}(\mathbf{C}_e)$ is the first invariant of right Cauchy-Green tensor \mathbf{C}_e .

4.2. Total potential energy and variational form

The general total potential energy of the nonlocal damage model is

$$\Pi = \int_{\Omega} \psi \, dV - \int_{\Omega} \bar{\mathbf{B}} \cdot \boldsymbol{\varphi} \, dV - \int_{\partial\Omega} \bar{\mathbf{T}} \cdot \boldsymbol{\varphi} \, dS, \quad (56)$$

where $\bar{\mathbf{B}}$ is the body force vector per unit reference volume of Ω and $\bar{\mathbf{T}}$ is the traction on the boundary $\partial\Omega$.

Minimization of the potential energy with respect to the primal variables $\boldsymbol{\varphi}$ and ϕ results in a coupled nonlinear system of equations that may be written as

$$\int_{\Omega} \mathbf{P} : \nabla_{\mathbf{X}} \delta \boldsymbol{\varphi} \, dV - \int_{\Omega} \bar{\mathbf{B}} \cdot \delta \boldsymbol{\varphi} \, dV - \int_{\partial\Omega} \bar{\mathbf{T}} \cdot \delta \boldsymbol{\varphi} \, dS = 0, \quad (57)$$

$$\int_{\Omega} \mathbf{Y} : \nabla_{\mathbf{X}} \delta \phi \, dV - \int_{\Omega} Y \delta \phi \, dV = 0, \quad (58)$$

where \mathbf{P} is the first Piola-Kirchhoff stress, \mathbf{Y} is vectorial damage quantity related to flux terms and Y is the scalar damage quantity associated to source terms. They are defined as

$$\mathbf{P} = \partial_{\mathbf{F}}\Psi, \quad \mathbf{Y} = \partial_{\nabla_{\mathbf{x}}\phi}\Psi, \quad Y = -\partial_{\phi}\Psi. \quad (59)$$

The corresponding spatial quantities in Eq. (59) are given by

$$\boldsymbol{\sigma} = \mathbf{P} \cdot \text{cof}(\mathbf{F}^{-1}), \quad \bar{\mathbf{b}} = J^{-1}\bar{\mathbf{B}}, \quad (60)$$

$$\mathbf{y} = \mathbf{Y} \cdot \text{cof}(\mathbf{F}^{-1}), \quad y = J^{-1}Y, \quad (61)$$

where $\text{cof}(\mathbf{F}) = J\mathbf{F}^{-\text{T}}$.

Substituting Eqs. (2) and (59) into Eqs. (57) and (58), the variational forms in the spatial description are

$$\int_{\Omega} \boldsymbol{\sigma} : \nabla_{\mathbf{x}}\delta\boldsymbol{\varphi} \, dv - \int_{\Omega} \bar{\mathbf{b}} \cdot \delta\boldsymbol{\varphi} \, dv - \int_{\partial\Omega} \bar{\mathbf{t}} \cdot \delta\boldsymbol{\varphi} \, ds, \quad (62)$$

$$\int_{\Omega} \mathbf{y} : \nabla_{\mathbf{x}}\delta\phi \, dv - \int_{\Omega} y\delta\phi \, dv = 0. \quad (63)$$

4.2.1. Finite element discretization

Isoparametric interpolations of the geometry variables \mathbf{X} , field variables $\boldsymbol{\varphi}$ and nonlocal field ϕ are respectively written as

$$\mathbf{X}^h = \sum_{I=1}^{n_{en}^{\mathbf{X}}} N_I(\xi)\mathbf{X}_I, \quad \boldsymbol{\varphi}^h = \sum_{I=1}^{n_{en}^{\boldsymbol{\varphi}}} N_I(\xi)\boldsymbol{\varphi}_I, \quad \phi^h = \sum_{I=1}^{n_{en}^{\phi}} N_I(\xi)\phi_I, \quad (64)$$

where ξ denotes the coordinates in the reference element, $n_{en}^{\boldsymbol{\varphi}}$ and n_{en}^{ϕ} are the nodal displacements and nodal nonlocal damage variables, respectively.

The FE interpolations of Eq. (64) are introduced into the coupled nonlinear system of Eqs. (62) and (63). To solve the coupled non-linear system of equations, an incremental-iterative Newton-Raphson-type scheme is adopted:

$$\begin{bmatrix} \mathbf{R}_{\boldsymbol{\varphi}} \\ \mathbf{R}_{\phi} \end{bmatrix}^i + \begin{bmatrix} \mathbf{K}_{\boldsymbol{\varphi}\boldsymbol{\varphi}} & \mathbf{K}_{\boldsymbol{\varphi}\phi} \\ \mathbf{K}_{\phi\boldsymbol{\varphi}} & \mathbf{K}_{\phi\phi} \end{bmatrix}^i \cdot \begin{bmatrix} \Delta\boldsymbol{\varphi} \\ \Delta\phi \end{bmatrix}^{i+1} = \begin{bmatrix} \mathbf{0} \\ \mathbf{0} \end{bmatrix}, \quad (65)$$

where

$$\mathbf{K}_{\boldsymbol{\varphi}\boldsymbol{\varphi}} = \int_{\Omega} \nabla_{\mathbf{x}}^T N \cdot [\mathbf{C}_h(d, t)] \cdot \nabla_{\mathbf{x}} N \, dv + \int_{\Omega} [\nabla_{\mathbf{x}}^T N \cdot \boldsymbol{\sigma} \cdot \nabla_{\mathbf{x}} N] \mathbf{I} \, dv, \quad (66)$$

$$\mathbf{K}_{\boldsymbol{\varphi}\phi} = \int_{\Omega} \nabla_{\mathbf{x}}^T N \cdot \frac{d\boldsymbol{\sigma}}{d\phi} \cdot N \, dv, \quad (67)$$

$$\mathbf{K}_{\phi\boldsymbol{\varphi}} = \int_{\Omega} N^T \cdot 2 \frac{dy}{dg} \cdot \nabla_{\mathbf{x}}^T N \, dv, \quad (68)$$

$$\mathbf{K}_{\phi\phi} = \int_{\Omega} N^T \cdot \frac{d\mathbf{y}}{d\phi} \cdot N dv + \int_{\Omega} \nabla_{\mathbf{x}}^T N \cdot \frac{d\mathbf{y}}{d\phi} \cdot \nabla_{\mathbf{x}}^T N dv. \quad (69)$$

In the above equations the tangent terms $d\boldsymbol{\sigma}/d\phi$, $2d\mathbf{y}/d\mathbf{g}$, $d\mathbf{y}/d\phi$ and $d\mathbf{y}/d\phi$ are similar to the ones derived by Waffenschmidt et al. [19] and Polindara et al. [20], and $\mathbf{C}_h(d, t)$ is a new time-dependent tangent stress-strain matrix in the damage and healing process given by

$$\mathbf{C}_h(d, t) = 4f(d)(1 - \lambda) \frac{\partial^2 \psi_{e11}(\mathbf{C}_e)}{\partial \mathbf{C}_e \partial \mathbf{C}_e} + 4\lambda \frac{\partial^2 \psi_{e12}(\mathbf{C}_e)}{\partial \mathbf{C}_e \partial \mathbf{C}_e}, \quad (70)$$

where the detailed expressions of $\frac{\partial^2 \psi_{e11}(\mathbf{C}_e)}{\partial \mathbf{C}_e \partial \mathbf{C}_e}$ and $\frac{\partial^2 \psi_{e12}(\mathbf{C}_e)}{\partial \mathbf{C}_e \partial \mathbf{C}_e}$ can be found in Nolan et al. [18].

5. Numerical examples

The model proposed in this paper is implemented within the commercial FE software Abaqus/Standard by means of a user subroutine UEL. Three numerical examples are shown onwards to illustrate the damage and healing effects in soft tissues with this model. In each example, an exponential damage function $f(d) = e^{-d}$ is adopted, but any other damage function satisfying Eq. (38) could be used. In both examples, the subscript 1 indicates the damaged tissues and 2 denotes the newly deposited part. Moreover, only the assumptions that the material properties of the newly deposited part are the same as the original tissues are considered in the following simulations.

5.1. Uniaxial tension

The first example is shown in Fig. 1. A square plate with a 10 mm edge length is subjected to uniaxial tensile loading. As shown in Fig. 1(b), the displacement increases continuously from 0-100 days and is kept constant after the 100th day. The G&R process is assumed to start from time $t=100$ days, and only one finite element is used in this example. The detailed material parameters are shown in Table 1. The physiological potential of original tissues is set as $\Delta\psi_{ph1} = 0.001 J$ in this example.

Firstly, we check the the performance of the proposed model in simulating growth. Three values of growth limit r_{g1} are set: $r_{g1} = \|\mathbf{q}_{g1}\|_{t=10 \text{ days}}$, $r_{g1} = \|\mathbf{q}_{g1}\|_{t=20 \text{ days}}$ and $r_{g1} = \|\mathbf{q}_{g1}\|_{t=50 \text{ days}}$. The growth rate is $M_{g1} = 0.01 \text{ day}^{-1}$ and no remodeling is assumed to occur by setting $M_{rm} = 0$. The variations of the Cauchy stress σ_x and the displacement u_y with time in Figs. 2(a) and 2(b) demonstrate that different homeostatic states can be reached by changing the growth limit r_{g1} , and a larger value of the r_{g1} (in three values introduced above) leads to a larger homeostatic stress (see from Fig. 2(a)) and a smaller displacement (see u_y from Fig. 2(b)), it can be explained that a smaller gap between homeostatic and current state is produced by a larger r_{g1} , therefore, a smaller growth deformation is required in the healing process. Figs. 3(a) and 3(b) show the influence of the growth rate M_{g1} and it shows that a larger growth rate leads to a faster convergence of the homeostatic state.

Secondly, the performance of the proposed model in simulating remodeling without growth are shown in Figs. 4 and 5. Three different values of the rate of remodeling M_{rm} are

tested to check the influence of the remodeling rate M_{rm} with the irreversible stiffness loss $\eta = 0$. The results of the variations of σ_x and $H(d, t)$ with time shown in Figs. 4(a) and 4(b) illustrate that a higher value of the remodeling rate M_{rm} induces a faster remodeling speed, which means a shorter time is needed in the process of replacement of the damaged tissues by the newly deposited part. The influence of the irreversible stiffness loss η on the variations of σ_x and $H(d, t)$ with time are shown in Figs. 5(a) and 5(b) by setting four different values, i.e., $\eta = 0$, $\eta = 0.2$, $\eta = 0.5$ and $\eta = 1.0$, when $M_{rm} = 0.01 \text{ days}^{-1}$, it is seen that the converged healing parameter $H(d, t)$ gradually increases with the decrease of η , and $H(d, t)$ converges to 1 when $\eta = 0$ indicating a complete healing for soft tissue, while $H(d, t)$ converges to 0 meaning no healing occurs when $\eta = 1$.

Thirdly, the combined effects of growth and remodeling are shown in Fig. 6. The G&R parameters are set as follows: $r_{gi} = \|(\mathbf{q}_{gi})\|_{t=10 \text{ days}}$, $M_{g1} = M_{g2} = 0.03 \text{ days}^{-1}$, $M_{rm} = 0.01 \text{ days}^{-1}$ and $\eta = 0$. In Figs. 6(a) and 6(b), the variations in σ_x and u_y with time are shown by comparing three cases: (1) Only growth occurs; (2) only remodeling occurs; and (3) growth and remodeling occur at the same time. The result in Fig. 6(a) illustrating that, when growth and remodeling combined occur, the stress decreases firstly due to the change in the configuration caused by growth and with the remodeling of the damaged tissues, and the stress increases until all damaged tissues are changed into the newly deposited part, and finally, the stress converges to a different homeostatic stress compared to the situation where only growth occurs. Although remodeling does not change the homeostatic stress much (see from Fig. 6(a)), a larger u_y can be found in Fig. 6(b) by comparing with case (1) and (3), and that can be illustrated by the combined effects of G&R such that a larger deformation is needed for the newly deposited part to converge to the homeostatic state than for the damaged part.

5.2. Open-hole plate

The second numerical example is an open-hole plate subjected to displacement loading. The geometry and the loading curve are shown in Fig. 7. The detailed material parameters are reported in Table 2. Due to the symmetry, only 1/4 of the plate at the top right corner is analyzed. For all simulations, the irreversible stiffness loss parameter $\eta = 0$.

Firstly, the mesh dependence of the proposed method is investigated by simulating three different mesh sizes (79 elements, 286 elements, and 793 elements), and the average Cauchy stress σ_x of the right side and the contours for the healing parameter $H(d, t)$ at different time are shown in Fig. 8 and Fig. 9, respectively. The G&R parameters are set as $M_{gi} = 0.03 \text{ days}^{-1}$, $M_{rm} = 0.1 \text{ days}^{-1}$ and $r_{gi} = \|(\mathbf{q}_{gi})\|_{t=50 \text{ days}}$, respectively. Both the stress curves and contours of the healing parameter illustrate that the results are rather similar for all different elements used, and a good mesh-independence is achieved by the proposed model.

Secondly, the influence of different G&R parameters are analyzed. The sensitivity of parameters of G&R M_{rm} , M_{g1} and M_{g2} are set as four different values with the growth limit $r_{gi} = \|(\mathbf{q}_{gi})\|_{t=50 \text{ days}}$. It can be seen from Fig. 10(a) that the Cauchy stress σ_x can converge to the homeostatic state for all four cases, and a larger remodeling rate M_{rm} induces a higher stress in the healing process when the growth rate M_{gi} is same. Although the remodeling

rate M_{rm} has relatively less influence on the homeostatic stress (see from Fig. 10(a)), the long-term evolution of the deformation is still depended on the remodeling rate M_{rm} , which can be seen from Fig. 10(b) that the displacement at node A (the location is shown in Fig. 7(a)) is shown. It is seen in Fig. 10(b) that, at the beginning of G&R, a faster decrease of the displacement is caused by a higher growth rate, and as for the homeostatic state, a higher remodeling rate M_{rm} leads to a larger deformation u_y with the same M_{gi} , while a larger deformation u_y is produced with a smaller M_{gi} when M_{rm} is the same.

The influence of growth limit is also investigated under three different values, i.e., $r_{gi} = \|\mathbf{q}_{gi}\|_{t=30 \text{ days}}$, $r_{gi} = \|\mathbf{q}_{gi}\|_{t=40 \text{ days}}$ and $r_{gi} = \|\mathbf{q}_{gi}\|_{t=50 \text{ days}}$, and the average Cauchy stress σ_x of the right side and the displacement u_y at node A (the location is shown in Fig. 7(a)) are shown in Fig. 11(a) and Fig. 11(b), respectively. The G&R rate are set as $M_{gi} = 0.03 \text{ days}^{-1}$ and $M_{rm} = 1.0 \text{ days}^{-1}$, respectively. All three different r_{gi} can converge to the homeostatic state, and the homeostatic stress increases with increasing the growth limit. Combining Figs. 11(a) and 11(b), it can be found that a smaller displacement is produced when there exists a smaller gap between the current state and the homeostatic state to recover.

Thirdly, the evolution of the contours of the healing parameter $H(d, t)$, the volume ratio of the newly deposited part λ , and the component of the growth deformation for the damaged part $F_{g1}(1, 1)$ and the newly deposited part $F_{g2}(1, 1)$ through the healing process are shown in Fig. 12(a)-(d), respectively, when $M_{gi} = 0.03 \text{ days}^{-1}$, $M_{rm} = 0.1 \text{ days}^{-1}$ and $r_{gi} = \|\mathbf{q}_{gi}\|_{t=50 \text{ days}}$. It can be observed that growth mainly occurs before the 500th day in this example, while remodeling occurs for a relatively longer time, which is similar to the results shown in Fig. 10. The contours shown in Fig. 12 exhibit the ability of our proposed model in predicting the evolution of G&R over the long-term time again.

5.3. Balloon angioplasty in atherosclerotic artery

The third example is associated with intraoperative injury and the long-term healing of atherosclerotic patients. The idealized two-dimensional cross-sectional model shown in Fig. 13 was established by Loree et al. [21]. The artery is modeled as a thick-walled cylinder with an inner radius of 1.8 mm and an outer radius of 2.0 mm. The lumen is modeled as a circular hole of radius 1.0 mm with an eccentricity of 0.5 mm with respect to the artery center. Fibrous plaque occupies the region between the luminal wall and the inner wall of the artery. The fibrous cap is assumed as continuous with the fibrous plaque and has the same material properties as the fibrous plaque. A subintimal lipid pool exists as a 140° crescent with an inner radius of 1.25 mm and outer radius of 1.75 mm with respect to the lumen center. The detailed material parameters reported in Table 3 are taken from Gasser et al. [22]. Due to the symmetry, only half of the model is analyzed.

The only boundary conditions are the nodal displacements of the inner luminal nodes. A radial displacement loading is imposed on each node from its initial position, $r_i = 1.0 \text{ mm}$, to give a final deformed radius, $r_f = 1.4 \text{ mm}$, and to maintain the deformation in the healing process. The displacement loading is applied within 100 steps and G&R is assumed to be started after displacement loading. The growth limit is set to the value of the determinant of the driven force of growth when the radius of lumen is $r_l = 1.2 \text{ mm}$, as $r_{gi} = \|\mathbf{q}_{gi}\|_{r_l=1.2 \text{ mm}}$.

The performance of the proposed model is tested by simulating the variations in four healing related parameters, $H(d, t)$, λ , $F_{g1}(1, 1)$ and $F_{g2}(1, 1)$, as shown in Fig. 14. The results of $H(d, t)$ in Fig. 14(a) show that the damage initially mainly occurs at the fiber cap in the shoulder of the plaque, the results agree with the review report of Holzapfel et al. [23]. The variation of $H(d, t)$ from 0 day to 400 day shown in Fig. 14(a) demonstrates that the damage in balloon angioplasty can be partly healed over a long-term time, for instance, the minimum value of the healing parameter $H(d, t)$ in the entire domain is increasing from 0.46 to 0.83 in this example. Moreover, it is interesting that our proposed model provides the variations of more parameters during the healing process at the same time, for instance, the results of λ shown Fig. 14(b) indicates that the position where the new tissue is produced is almost the same with the position where the damage occurred. The component of the growth deformation for the original $F_{g1}(1, 1)$ and the newly deposited tissues $F_{g2}(1, 1)$ are also shown in Fig. 14(c) and Fig. 14(d), respectively, which illustrate the influence of growth on deformation in the healing process.

To further investigate the evolution of G&R at specific positions, four nodes (the locations shown in Fig. 13) are selected, and the Von Mises stress σ_m and the magnitude of displacement $u_m = \sqrt{u_x^2 + u_y^2}$ are calculated as shown in Fig. 15. The curves of the variations of σ_m and u_m with time shown in Fig. 15 illustrate that the proposed model works well and can converge to the homeostatic state.

As the inflation size is the critical indicator in balloon angioplasty [24], two inflation sizes are tested to investigate the influence of the inflation size on G&R, as the contours of the healing parameter $H(d, t)$ and the the volume ratio of the newly deposited part λ are shown in Fig. 16. The minimum value of the healing parameter $H(d, t)$ at [0, 100, 200, 400] days is [0.46, 0.82, 0.83, 0.83] when $r_f = 1.40$ mm compared with the corresponding results of $H(d, t)$ is [0.17, 0.74, 0.77, 0.79] when $r_f = 1.48$ mm. Although a faster healing speed can be observed at the beginning of the healing process when $r_f = 1.48$ mm, a larger area of unrecoverable damage remains when healing is completed. Therefore, the long-term evolution of the damage is also important and must be considered. Fig. 17 shows the evolution of the normalized outer artery radius $R(t)$ in the healing process, obtained by calculating the time-dependent ratio of the outer radius of the artery $R(t) = \frac{r_{oa}(t)}{r_{oa}(t=0)}$, where r_{oa} is the outer radius of the artery. The variations of $R(t)$ shown in Fig. 17 demonstrates that the artery wall gradually changes to be thicker during the healing process and finally converges to a stable thickness at homeostatic state, this phenomenon is similar to the computational results by Braeu et al. in simulating of the thickening of arterial wall in hypertension [25]. It can be explained that thickening of the wall helps restore a homeostatic state, as it decreases the wall stress back to the initial level [25]. A smaller deformation for $r_f = 1.48$ mm can be illustrated by a larger unrecoverable damage, which means that litter displacement is needed to recover to the homeostatic stress state, similar to the results in Example 2.

6. Conclusions

Based on the framework of thermodynamics, a new unified continuum damage model of the healing of soft biological tissues is proposed for the first time in this paper. Different from the existing damage models of soft tissue healing, all the parameters related to the healing process can be regarded as the internal variables, in the same way as the damage variable. Therefore, the evolution of these healing parameters can be strictly derived based on the theory of thermodynamics, and thus, no *ad hoc* equations are required as in the existing healing models. By virtue of the proposed unified damage models, the difficulty caused by the models available in the literature, for example, their disregard of continuum mechanical requirements such as that material frame indifference, explicit time dependence of material parameters, or unclear meaning of parameters, can be well overcome.

The proposed unified continuum damage model is validated by three representative numerical examples. The basic performance of the proposed model is shown through a uniaxial tension scenario, the results of which show that the proposed model can well simulate the healing process, including the occurrence of damage and the recovery process. In addition, the evolution of the volume ratio of the newly deposited tissue and the growth deformation can be well illustrated. The nonlocal healing of the proposed model is achieved by a combination of the gradient terms, good mesh independence is shown in the open-hole plate scenario, and the evolution of the volume ratios and growth deformations for both the original part and the newly deposited part for soft tissue is illustrated. The good potential of the method is demonstrated by a case of balloon angioplasty in the atherosclerotic artery with a fiber cap, where the long-term healing process in soft biological tissues after damage is simulated. The numerical results of the proposed model agree well with the existing works in indicating the occurring position of damage for artery [23] and predicting the trend of variation for arterial thickness in healing process [25].

The presented model is limited to 2D cases and to isotropic hyperelastic models. As collagen fibers are essential in the healing of soft tissue, the development of a 3D anisotropic model is currently in progress to address more realistic applications. The identification of newly defined healing parameters in the proposed unified model is also critical for applications to practical problems and is currently underway.

In summary, a new unified continuum damage model for the healing of soft biological tissues is presented in this paper. The evolution equations of healing parameters are derived based on the theory of thermodynamics. The proposed model provides a concise and rigorous framework for the establishment of a constitutive relationship and an *in silico* simulation of the healing of soft biological tissues with newly derived parameters having clear physical interpretations. The proposed model will be useful in simulating the entire surgery and recovery process of individual patients based on CT or MRI data, particularly in evaluating the risks and probability of carrying out surgical intervention.

Declaration of Competing Interest

The authors declare no competing interests.

CRedit author statement

Di Zuo: Software; Validation; Writing-Original Draft. **Yiqian He:** Supervision; Conceptualization; Writing-Review & Editing. **Stéphane Avril:** Writing-Review & Editing. **Haitian Yang:** Writing-Review & Editing. **Klaus Hackl:** Conceptualization; Methodology; Writing-Review & Editing.

Acknowledgments

The research leading to this paper was funded by the NSFC Grant [12072063], ERC-2014-CoG-BIOLOCHANICS [647067], grants from the State Key Laboratory of Structural Analysis for Industrial Equipment [GZ19105, S18402], the Liaoning Provincial Natural Science Foundation [2020-MS-110]. Klaus Hackl gratefully acknowledges financial support by Dalian University of Technology via a Haitian Scholarship.

References

- [1] I. Rao, Modeling of growth and remodeling in soft biological tissues with multiple constituents, *Mechanics Research Communications* 38 (2011) 24–28.
- [2] T. C. Gasser, *Damage in Vascular Tissues and Its Modeling*, Springer International Publishing, Cham, pp. 85–118.
- [3] C. Valero, E. Javierre, J. García-Aznar, M. Gómez-Benito, A. Menzel, Modeling of anisotropic wound healing, *Journal of the Mechanics and Physics of Solids* 79 (2015) 80–91.
- [4] E. Comellas, T. C. Gasser, F. J. Bellomo, S. Oller, A homeostatic-driven turnover remodelling constitutive model for healing in soft tissues, *Journal of the Royal Society Interface* 13 (2016) 20151081.
- [5] B. D. Cumming, D. McElwain, Z. Upton, A mathematical model of wound healing and subsequent scarring, *Journal of The Royal Society Interface* 7 (2009) 19–34.
- [6] A. Buganza Tepole, E. Kuhl, Computational modeling of chemo-bio-mechanical coupling: a systems-biology approach toward wound healing, *Computer methods in biomechanics and biomedical engineering* 19 (2016) 13–30.
- [7] E. Javierre, P. Moreo, M. Doblaré, J. García-Aznar, Numerical modeling of a mechano-chemical theory for wound contraction analysis, *International journal of solids and structures* 46 (2009) 3597–3606.
- [8] R. C. Schugart, A. Friedman, R. Zhao, C. K. Sen, Wound angiogenesis as a function of tissue oxygen tension: a mathematical model, *Proceedings of the National Academy of Sciences* 105 (2008) 2628–2633.
- [9] E. Kuhl, K. Garikipati, E. M. Arruda, K. Grosh, Remodeling of biological tissue: mechanically induced reorientation of a transversely isotropic chain network, *Journal of the Mechanics and Physics of Solids* 53 (2005) 1552–1573.
- [10] J. Humphrey, K. Rajagopal, A constrained mixture model for growth and remodeling of soft tissues, *Mathematical models and methods in applied sciences* 12 (2002) 407–430.
- [11] M. Latorre, J. D. Humphrey, Critical roles of time-scales in soft tissue growth and remodeling, *APL bioengineering* 2 (2018) 026108.
- [12] B. Dimitrijevic, K. Hackl, A method for gradient enhancement of continuum damage models, *Technische Mechanik* 28 (2008) 43–52.
- [13] Y. He, D. Zuo, K. Hackl, H. Yang, S. J. Mousavi, S. Avril, Gradient-enhanced continuum models of healing in damaged soft tissues, *Biomechanics and modeling in mechanobiology* (2019) 1–18.
- [14] D. Zuo, S. Avril, H. Yang, S. J. Mousavi, K. Hackl, Y. He, Three-dimensional numerical simulation of soft-tissue wound healing using constrained-mixture anisotropic hyperelasticity and gradient-enhanced damage mechanics, *Journal of the Royal Society Interface* 17 (2020) 20190708.
- [15] C. B. Frank, N. G. Shrive, H. Hiraoka, N. Nakamura, Y. Kaneda, D. A. Hart, Optimisation of the biology of soft tissue repair, *Journal of Science and Medicine in Sport* 2 (1999) 190–210.
- [16] C. B. Frank, D. A. Hart, N. G. Shrive, Molecular biology and biomechanics of normal and healing ligaments—a review, *Osteoarthritis and Cartilage* 7 (1999) 130–140.
- [17] B. Dimitrijevic, K. Hackl, A regularization framework for damage–plasticity models via gradient enhancement of the free energy, *International Journal for Numerical Methods in Biomedical Engineering* 27 (2011) 1199–1210.
- [18] D. Nolan, A. Gower, M. Destrade, R. Ogden, J. McGarry, A robust anisotropic hyperelastic formulation for the modelling of soft tissue, *Journal of the mechanical behavior of biomedical materials* 39 (2014) 48–60.
- [19] T. Waffenschmidt, C. Polindara, A. Menzel, S. Blanco, A gradient-enhanced large-deformation continuum damage model for fibre-reinforced materials, *Computer Methods in Applied Mechanics and Engineering* 268 (2014) 801–842.
- [20] C. Polindara, T. Waffenschmidt, A. Menzel, A computational framework for modelling damage-induced softening in fibre-reinforced materials—application to balloon angioplasty, *International Journal of Solids and Structures* 118 (2017) 235–256.
- [21] H. M. Loree, R. Kamm, R. Stringfellow, R. T. Lee, Effects of fibrous cap thickness on peak circumferential stress in model atherosclerotic vessels., *Circulation research* 71 (1992) 850–858.

- [22] T. C. Gasser, G. A. Holzapfel, Modeling plaque fissuring and dissection during balloon angioplasty intervention, *Annals of biomedical engineering* 35 (2007) 711–723.
- [23] G. A. Holzapfel, J. J. Mulvihill, E. M. Cunnane, M. T. Walsh, Computational approaches for analyzing the mechanics of atherosclerotic plaques: A review, *Journal of Biomechanics* 47 (2014) 859–869.
- [24] A. N. Tenaglia, et al., Intravascular ultrasound and balloon percutaneous transluminal coronary angioplasty, *Cardiology clinics* 15 (1997) 31–38.
- [25] F. Braeu, A. Seitz, R. Aydin, C. Cyron, Homogenized constrained mixture models for anisotropic volumetric growth and remodeling, *Biomechanics and modeling in mechanobiology* 16 (2017) 889–906.

List of Tables

1	Material parameters for the uniaxial tension.	21
2	Material parameters for the open-hole plate.	22
3	Material parameters for the balloon angioplasty.	23

Table 1: Material parameters for the uniaxial tension.

Type	Description	Symbol	Values	Units
Hyperelastic	Shear modulus	μ_1	1	MPa
		μ_2	1	MPa
	Bulk modulus	k_1	1	MPa
		k_2	1	MPa
Damage	Damage threshold	κ_d	0.2	MPa
	Degree of regularisation	c_d	1	MPa \cdot mm ²
	Penalty parameter	β_d	0.001	MPa
	(Non)local switch	γ_d	1	-
Remodeling	Remodeling rate	M_{rm}	[0.01,0.02,0.05]	day ⁻¹
	Irreversible stiffness loss	η	[0,0.2,0.5,1.0]	-
Growth	Growth rate	M_{g1}	[0.01,0.02,0.05]	day ⁻¹
		M_{g2}	[0.01,0.02,0.05]	day ⁻¹
	Growth limit	r_{g1}	-	-
		r_{g2}	-	-

Table 2: Material parameters for the open-hole plate.

Type	Description	Symbol	Values	Units
Geometry	Height	H	100	mm
	Width	W	100	mm
	Diameter	R	50	mm
Hyperelastic	Shear modulus	μ_1	1	MPa
		μ_2	1	MPa
	Bulk modulus	k_1	40	MPa
		k_2	40	MPa
Damage	Damage threshold	κ_d	0.01	MPa
	Degree of regularization	c_d	1	MPa·mm ²
	Penalty parameter	β_d	1	MPa
	(Non)local switch	γ_d	1	-
Remodeling	Remodeling rate	M_{rm}	[0.1,1.0]	day ⁻¹
	Irreversible stiffness loss	η	0	-
Growth	Growth rate	M_{g1}	[0.01,0.03]	day ⁻¹
		M_{g2}	[0.01,0.03]	day ⁻¹
	Growth limit	r_{g1}	-	-
		r_{g2}	-	-

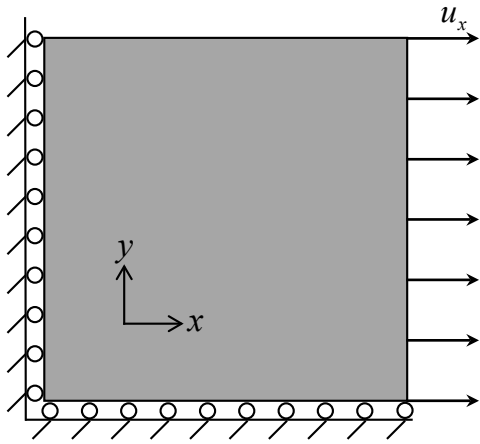
Table 3: Material parameters for the balloon angioplasty.

Type	Description	Symbol	Values	Units
Hyperelastic	Shear modulus	μ_a	15	kPa
		μ_{p1}	78.9	kPa
		μ_{p2}	78.9	kPa
		μ_l	0.1	kPa
	Bulk modulus	k_a	4	kPa
		k_{p1}	23.7	kPa
		k_{p2}	23.7	kPa
		k_l	0.5	kPa
Damage	Damage threshold	κ_d	5	kPa
	Degree of regularization	c_d	1	kPa·mm ²
	Penalty parameter	β_d	20	kPa
	(Non)local switch	γ_d	1	-
Remodeling	Remodeling rate	M_{rm}	0.1	<i>day</i> ⁻¹
	Irreversible stiffness loss	η	1.0	-
Growth	Growth rate	M_{g1}	0.01	<i>day</i> ⁻¹
		M_{g2}	0.01	<i>day</i> ⁻¹
	Growth limit	r_{g1}	-	-
		r_{g2}	-	-

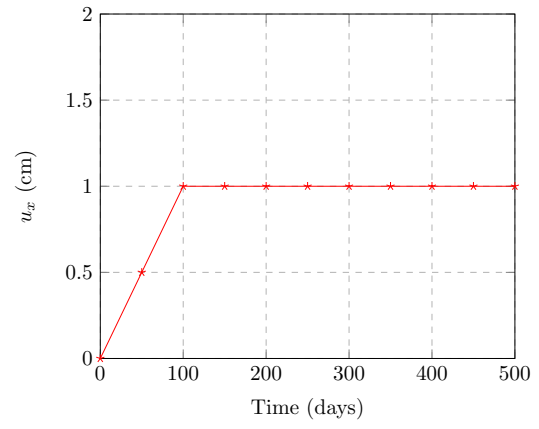
List of Figures

1	Geometry and displacement used in the uniaxial tensile case study. (a) Geometric model, and (b) Loading curve.	26
2	Influence of the growth limit r_{g1} in uniaxial tension. (a) The variation of the Cauchy stress σ_x with time, and (b) the variation of the displacement u_y with time.	27
3	Influence of the growth rate M_{g1} in uniaxial tension. (a) The variation of the Cauchy stress σ_x with time, and (b) the variation of the displacement u_y with time.	28
4	Influence of the healing rate M_{rm} in uniaxial tension. (a) The variation of the Cauchy stress σ_x with time (b) the variation of the healing parameter $H(d, t)$ with time.	29
5	Influence of the irreversible stiffness loss η in uniaxial tension. (a) The variation of the Cauchy stress σ_x with time, and (b) the variation of the healing parameter $H(d, t)$ with time.	30
6	Results for the uniaxial tensile test with different situations. (a) The variation of the Cauchy stress σ_x with time, and (b) the variation of the healing parameter $H(d, t)$ with time.	31
7	Geometry and loading condition for the open-hole plate case. (a) Geometry, (b) loading curve.	32
8	The average Cauchy stress σ_x of the right-hand side with different mesh sizes.	33
9	Variation of contours of the healing parameter $H(d, t)$ with time for different numbers of elements (a) 79 elements, (b) 286 elements, and (c) 793 elements.	34
10	Influence of the rate of G&R (M_{rm} , M_{g1} and M_{g2}) in open-hole plate. (a) The variation of the Cauchy stress σ_x with time, and (b) the variation of the displacement u_y with time at node A.	35
11	Influence of the growth limit r_{gi} in open-hole plate. (a) The variation of the Cauchy stress σ_x with time, and (b) the variation of the displacement u_y with time at node A.	36
12	The contours for different parameters in healing process at different times. (a) The healing parameter $H(d, t)$, (b) the newly deposited part λ , (c) the component of the growth deformation for damaged part $F_{g1}(1, 1)$, and (d) the component of the growth deformation for newly deposited part $F_{g2}(1, 1)$. . .	37
13	Geometric and FEM mesh model for balloon angioplasty.(a) Geometric model, and (b) FEM mesh model.	38
14	The contours for different parameters in healing process at different times. (a) The healing parameter $H(d, t)$, (b) the volume ratio of newly deposited part λ , (c) the component of the growth deformation for damaged part $F_{g1}(1, 1)$, and (d) the component of the growth deformation for the newly deposited part $F_{g2}(1, 1)$	39

15	Influence of the inflation size at different locations in balloon angioplasty. (a) The variation of the Von Mises stress σ_m with time, and (b) the variation of the displacement u_m with time.	40
16	The contours for different parameters and inflation size in healing process at different times. (a) The healing parameter $H(d, t)$ when $r_f = 1.40$ mm, (b) the healing parameter $H(d, t)$ when $r_f = 1.48$ mm, (c) the newly deposited part λ when $r_f = 1.40$ mm, (b) the newly deposited part λ when $r_f = 1.48$ mm.	41
17	The variations of $R(t)$ for different inflation size in balloon angioplasty. . . .	42



(a)



(b)

Figure 1: Geometry and displacement used in the uniaxial tensile case study. (a) Geometric model, and (b) Loading curve.

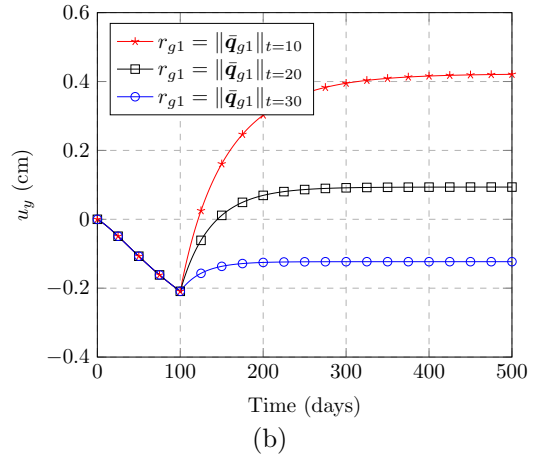
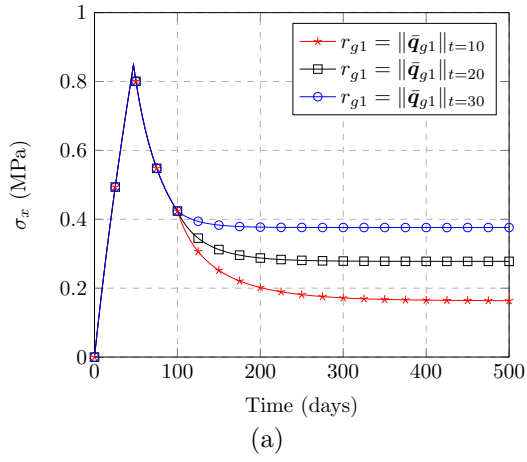


Figure 2: Influence of the growth limit r_{g1} in uniaxial tension. (a) The variation of the Cauchy stress σ_x with time, and (b) the variation of the displacement u_y with time.

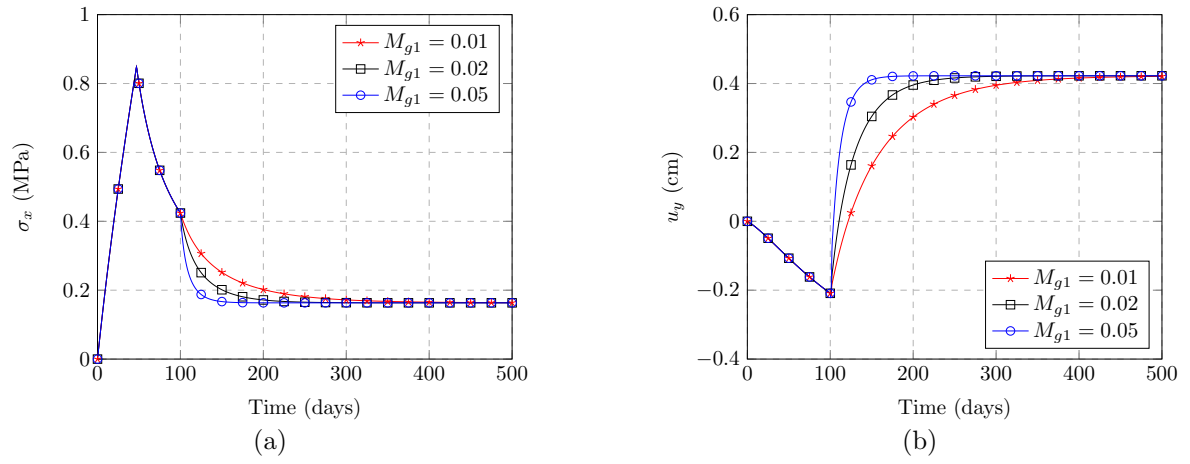


Figure 3: Influence of the growth rate M_{g1} in uniaxial tension. (a) The variation of the Cauchy stress σ_x with time, and (b) the variation of the displacement u_y with time.

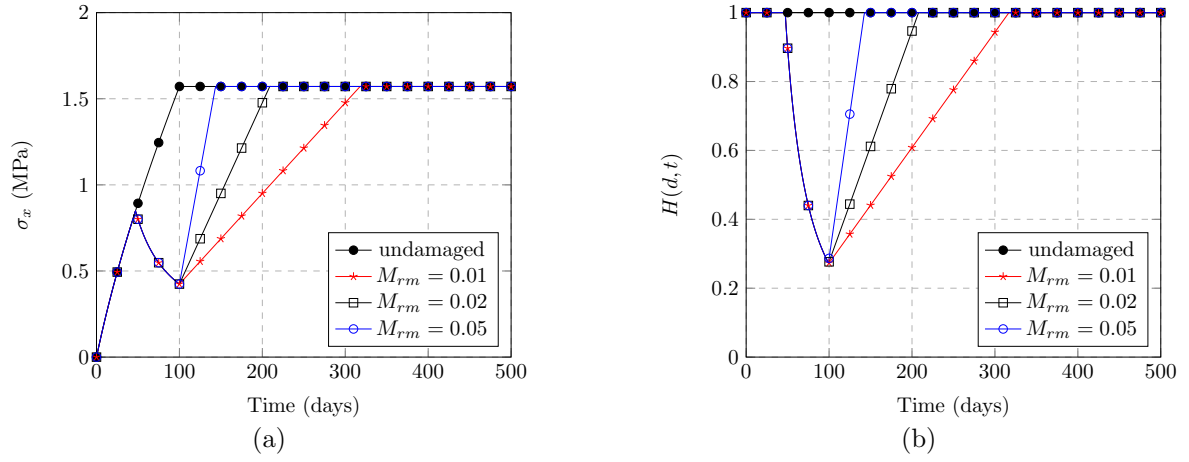


Figure 4: Influence of the healing rate M_{rm} in uniaxial tension. (a) The variation of the Cauchy stress σ_x with time (b) the variation of the healing parameter $H(d, t)$ with time.

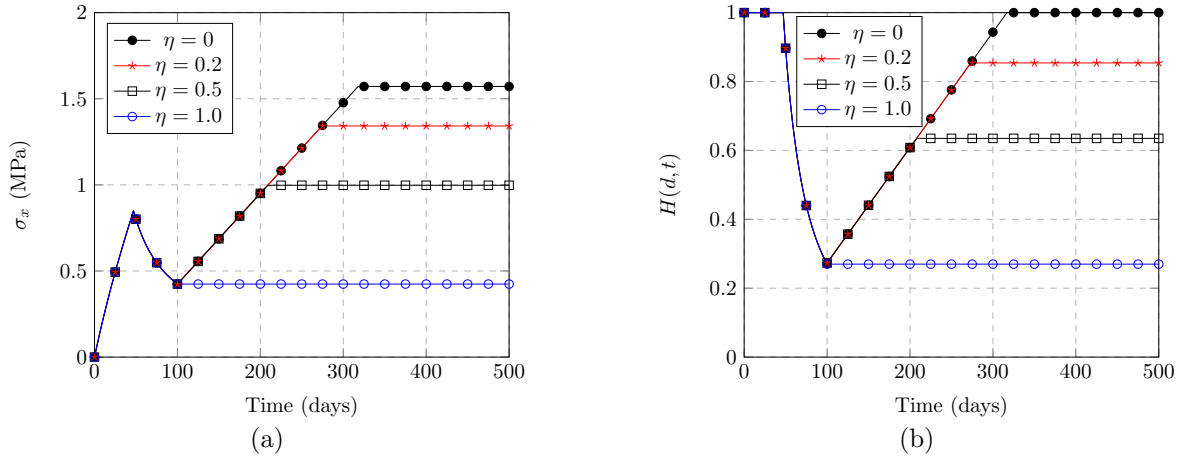


Figure 5: Influence of the irreversible stiffness loss η in uniaxial tension. (a) The variation of the Cauchy stress σ_x with time, and (b) the variation of the healing parameter $H(d, t)$ with time.

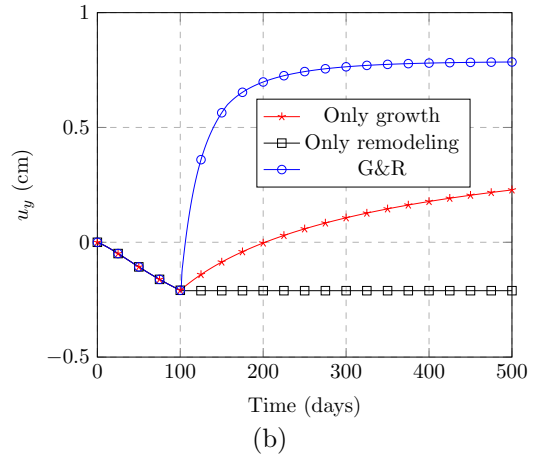
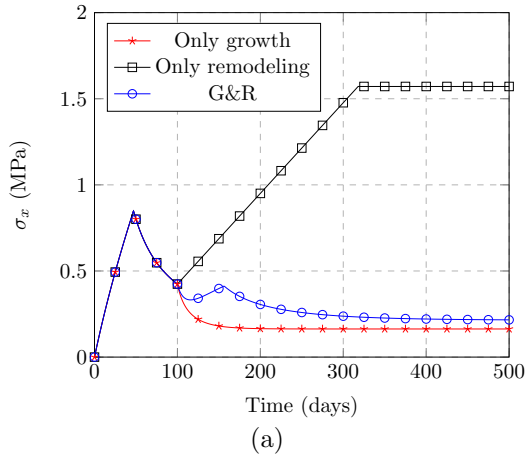


Figure 6: Results for the uniaxial tensile test with different situations. (a) The variation of the Cauchy stress σ_x with time, and (b) the variation of the healing parameter $H(d, t)$ with time.

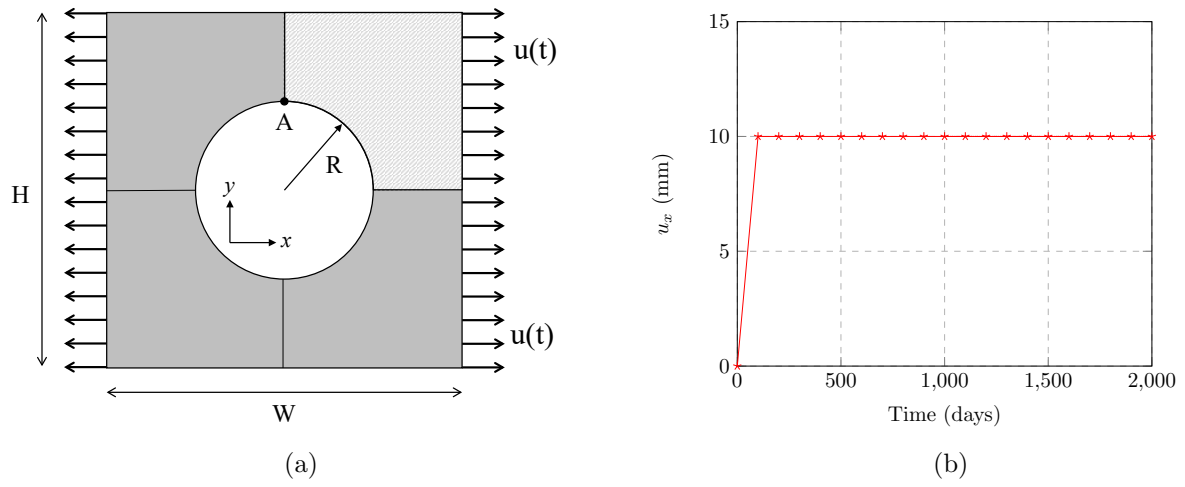


Figure 7: Geometry and loading condition for the open-hole plate case. (a) Geometry, (b) loading curve.

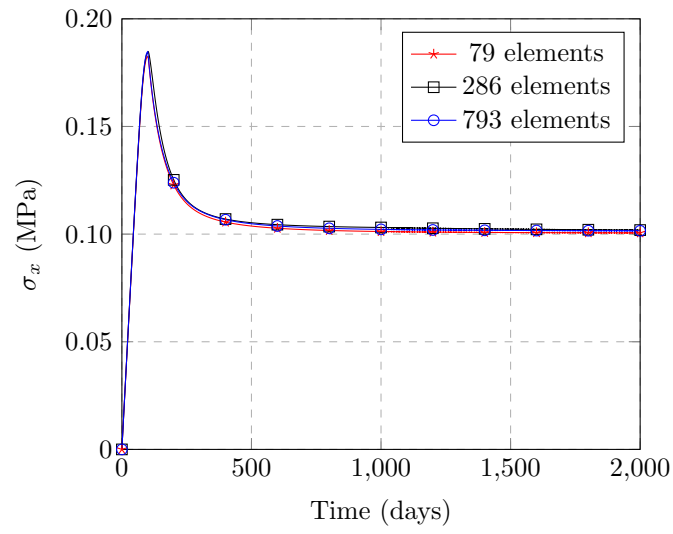


Figure 8: The average Cauchy stress σ_x of the right-hand side with different mesh sizes.

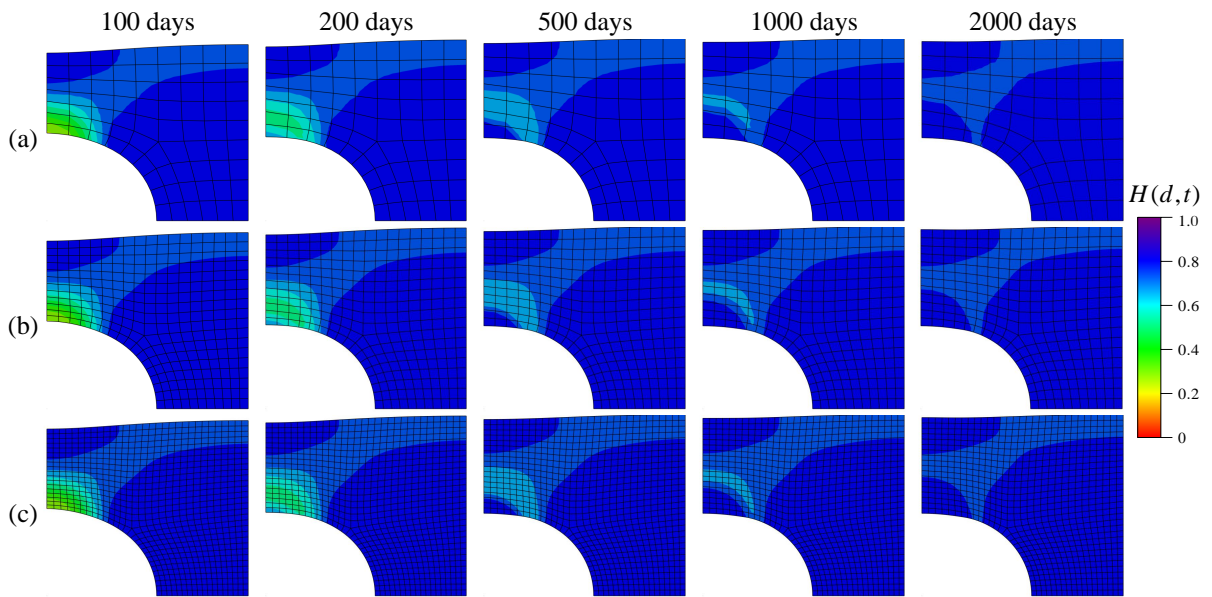


Figure 9: Variation of contours of the healing parameter $H(d,t)$ with time for different numbers of elements (a) 79 elements, (b) 286 elements, and (c) 793 elements.

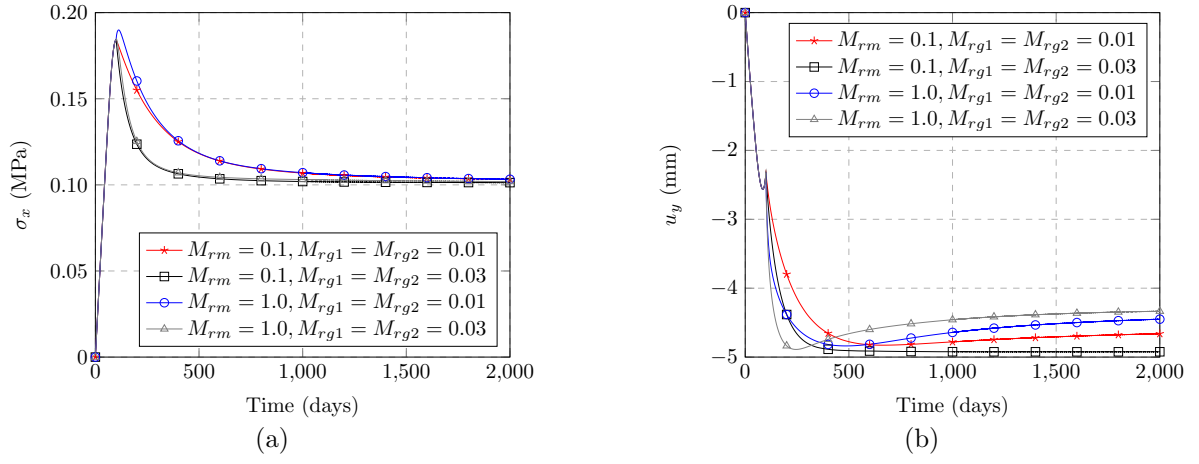


Figure 10: Influence of the rate of G&R (M_{rm} , M_{g1} and M_{g2}) in open-hole plate. (a) The variation of the Cauchy stress σ_x with time, and (b) the variation of the displacement u_y with time at node A.

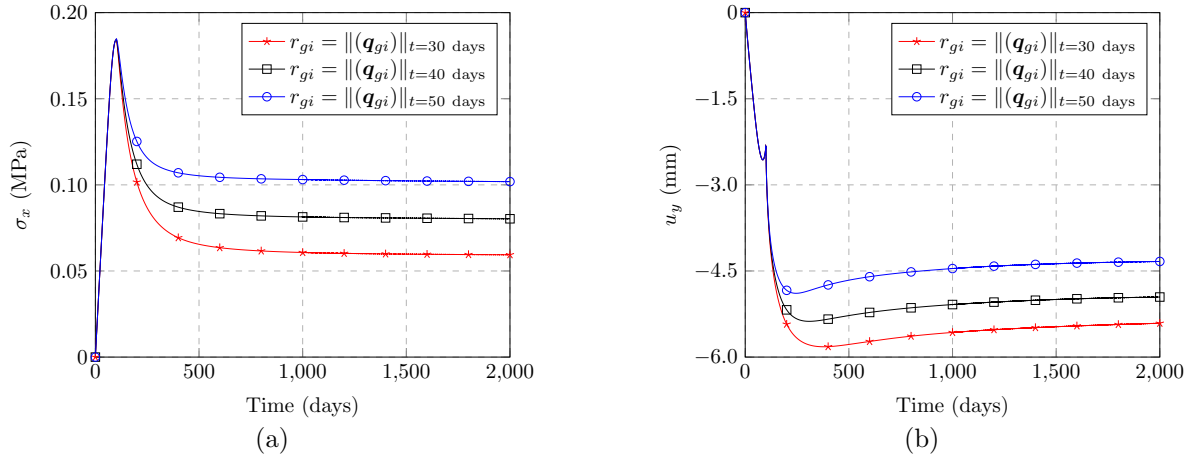


Figure 11: Influence of the growth limit r_{gi} in open-hole plate. (a) The variation of the Cauchy stress σ_x with time, and (b) the variation of the displacement u_y with time at node A.

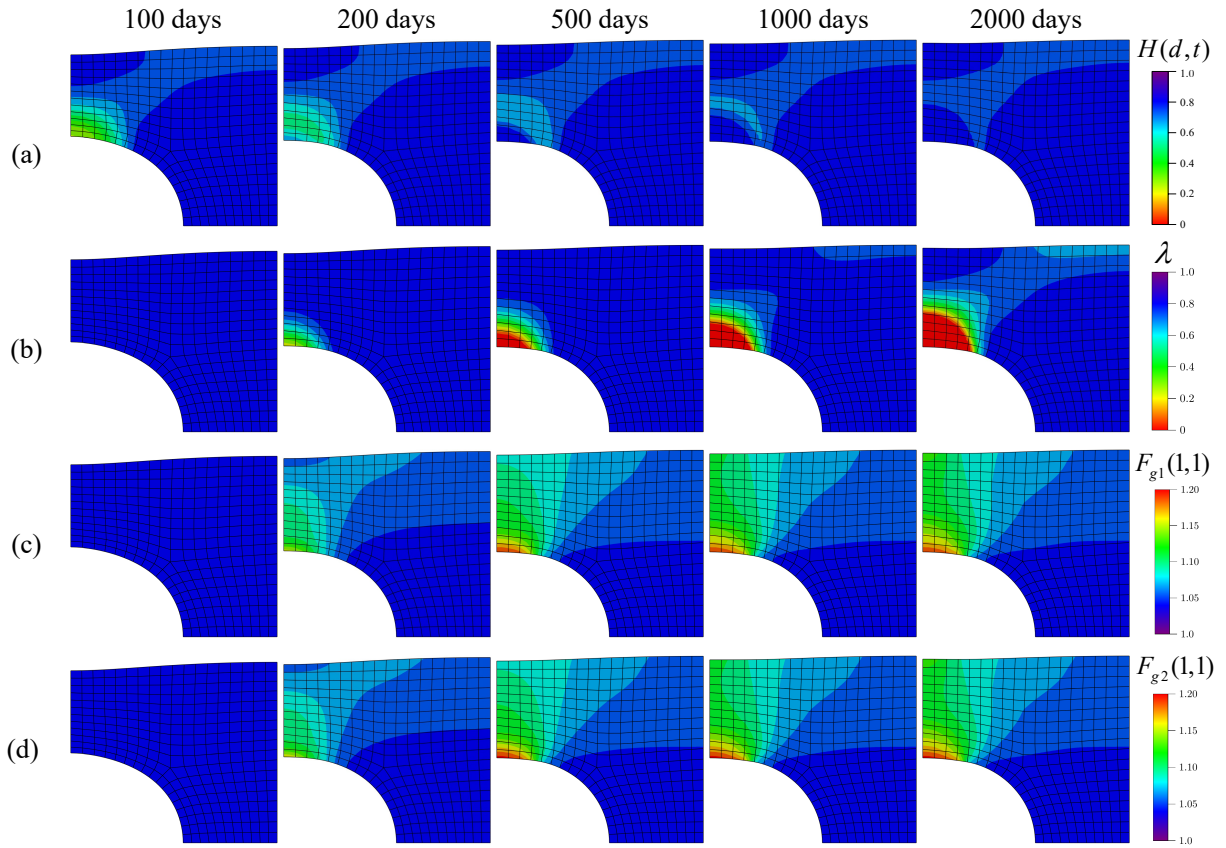


Figure 12: The contours for different parameters in healing process at different times. (a) The healing parameter $H(d,t)$, (b) the newly deposited part λ , (c) the component of the growth deformation for damaged part $F_{g1}(1,1)$, and (d) the component of the growth deformation for newly deposited part $F_{g2}(1,1)$.

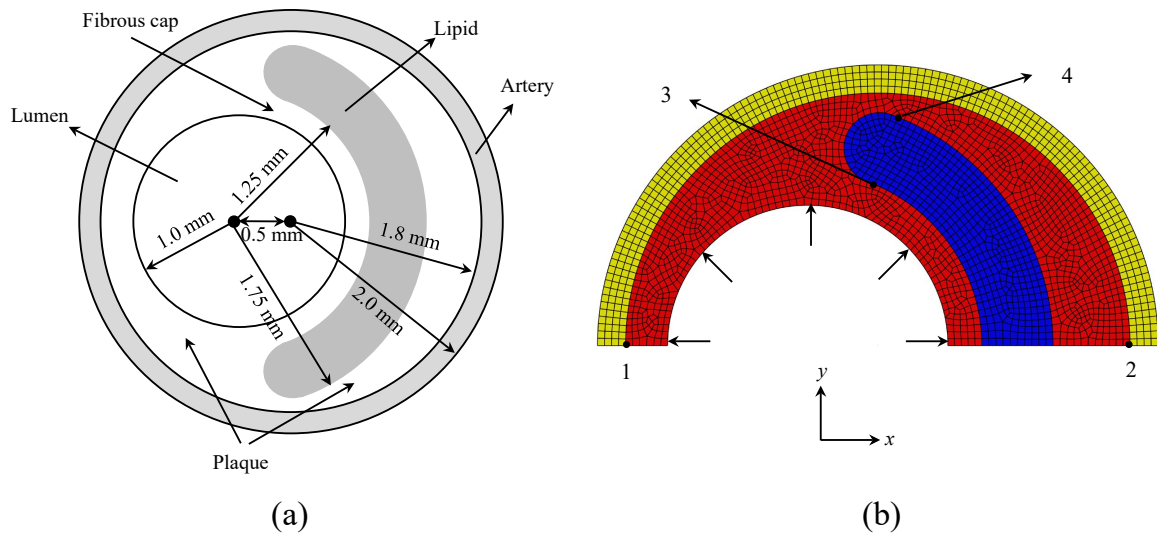


Figure 13: Geometric and FEM mesh model for balloon angioplasty.(a) Geometric model, and (b) FEM mesh model.

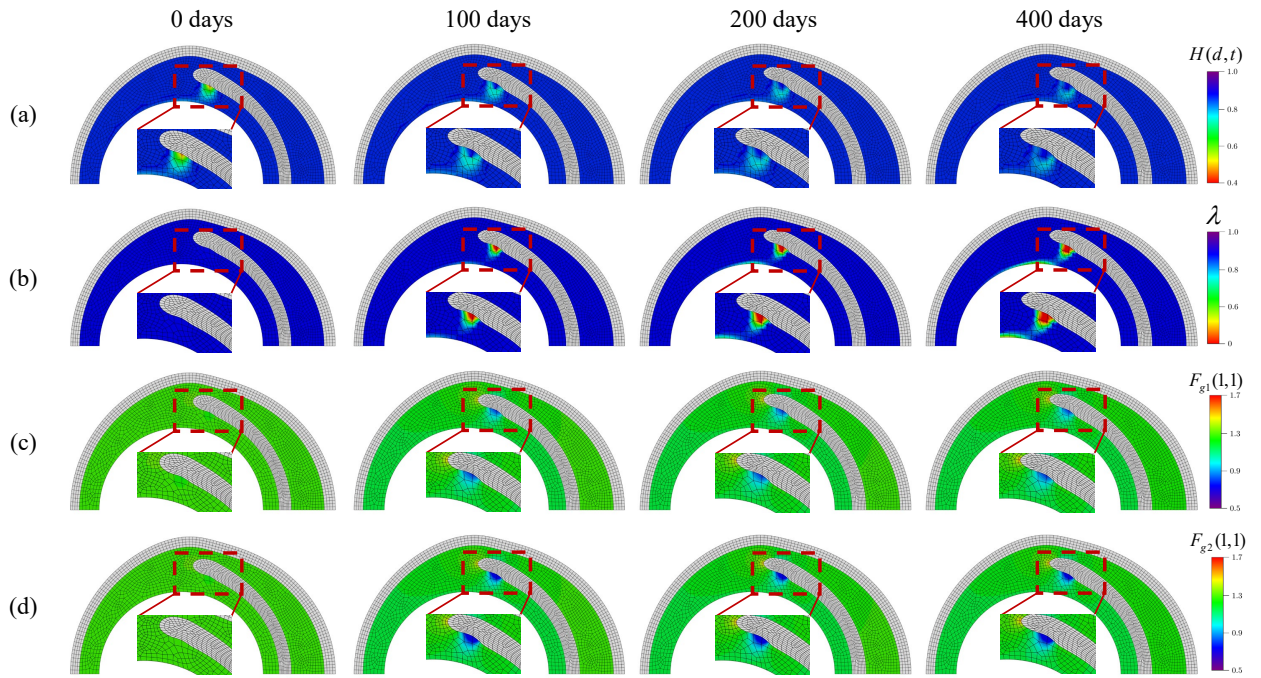


Figure 14: The contours for different parameters in healing process at different times. (a) The healing parameter $H(d, t)$, (b) the volume ratio of newly deposited part λ , (c) the component of the growth deformation for damaged part $F_{g1}(1, 1)$, and (d) the component of the growth deformation for the newly deposited part $F_{g2}(1, 1)$.

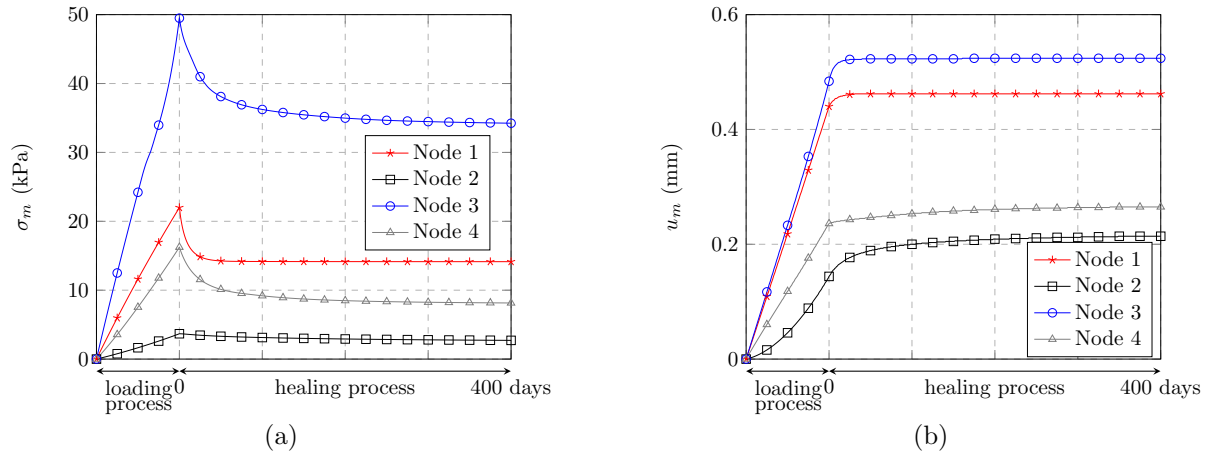


Figure 15: Influence of the inflation size at different locations in balloon angioplasty. (a) The variation of the Von Mises stress σ_m with time, and (b) the variation of the displacement u_m with time.

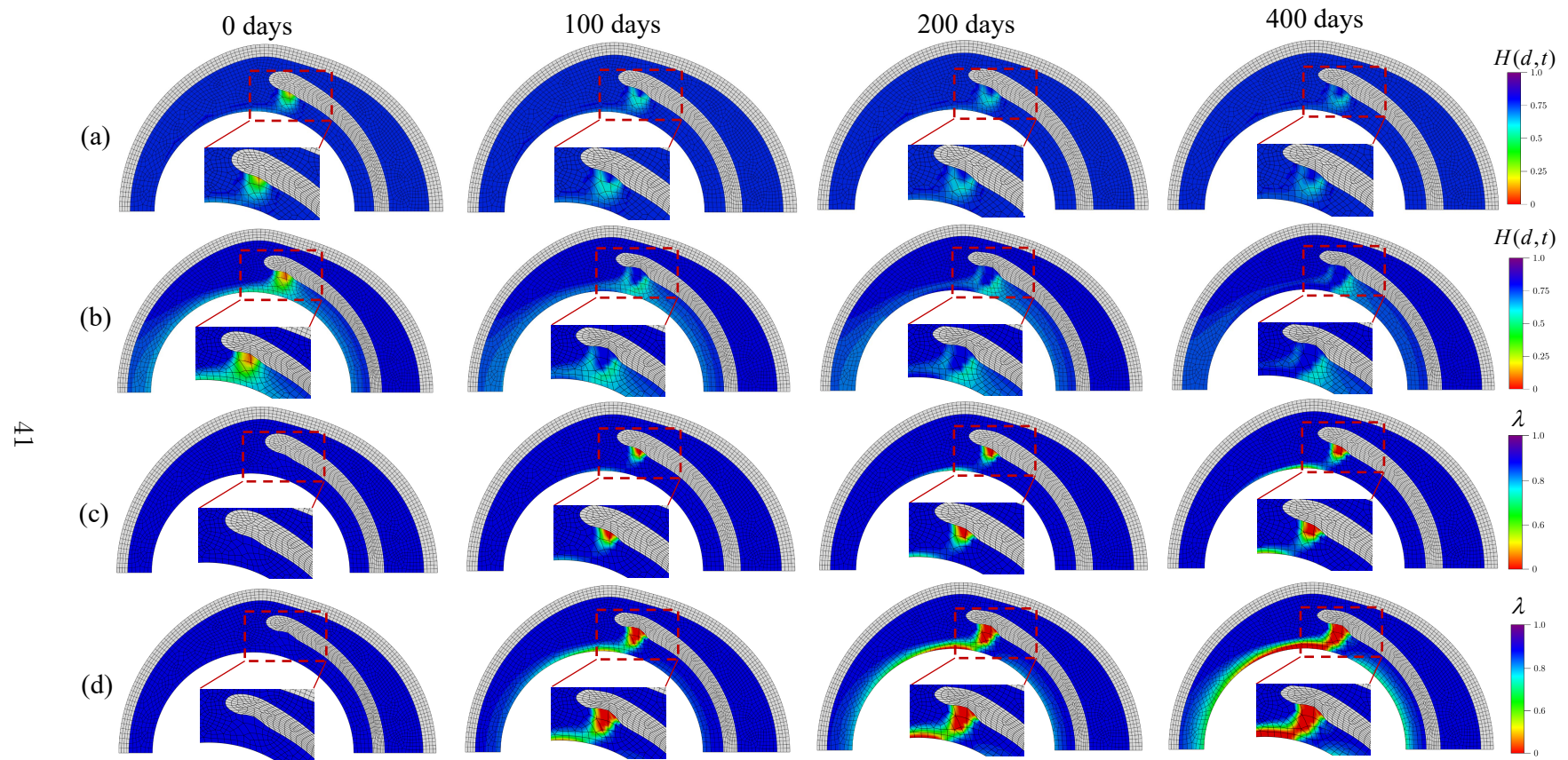


Figure 16: The contours for different parameters and inflation size in healing process at different times. (a) The healing parameter $H(d,t)$ when $r_f = 1.40$ mm, (b) the healing parameter $H(d,t)$ when $r_f = 1.48$ mm, (c) the newly deposited part λ when $r_f = 1.40$ mm, (d) the newly deposited part λ when $r_f = 1.48$ mm.

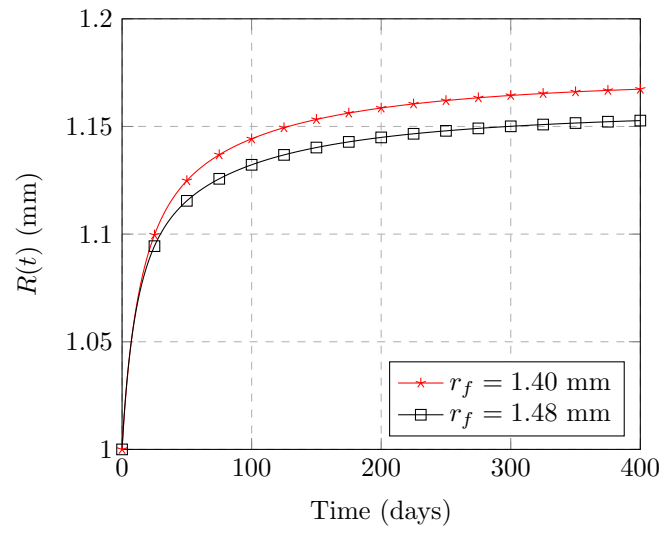


Figure 17: The variations of $R(t)$ for different inflation size in balloon angioplasty.